Electronic Supplementary Material (ESI) for Journal of Materials Chemistry A.

Supporting Information

Synergistic self-assembled 3D PEDOT:PSS/graphene composite sponge for stretchable microsupercapacitors

Wenrong Yan[ab], Jinhui Li[a], Guoping Zhang[b], Lei Wang*[b] and Derek HO*[a]

[a] *Department of Materials Science and Engineering, City University of Hong Kong,*

83 Tat Chee Avenue, Kowloon, Hong Kong 999077, China.

[b] *Shenzhen Institutes of Advanced Technology Chinese Academy of Sciences,*

Shenzhen 518055, China.

Corresponding authors:

Email: derekho@cityu.edu.hk (D. Ho), and wang.lei@siat.ac.cn (L. Wang).

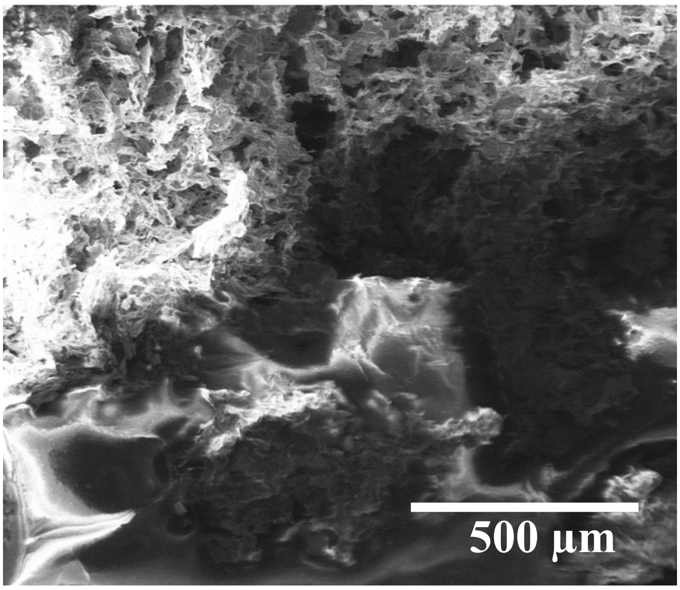

Figure S1. SEM image of 3D PGCS on silicone rubber.

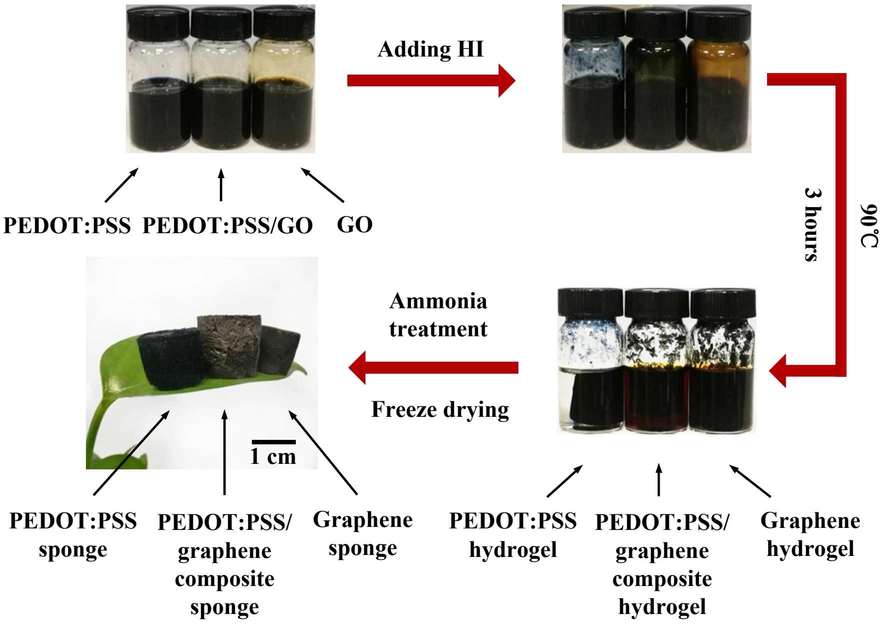

Figure S2. Reaction and synergistic self-assembly process of PGCHs and PGCSs from a 6 mg ml^{-1} PEDOT:PSS/GO mixture under HI treatment in conventional glass bottles.

Figure S2 shows that, during the reaction process, due to the reduction with GO, the PEDOT:PSS/GO solution becomes darker at first. Then, due to the self-assembly of both PEDOT and rGO, a hydrogel is formed in the solution,. After reacting for 3 h under 90 °C, the self-assembly process is fully complete. In the bottle of PEDOT:PSS hydrogel, it is evident that the solution is colorless and transparent, further verifying the forming dissoluble and colorless PSSH due to the bonding of H^{+} of HI with PSS chains. The dark brown solution in the bottle of both the PEDOT:PSS/graphene hydrogel and graphene hydrogel is due to the resultant iodine in the solution, due to the reaction of HI and GO.

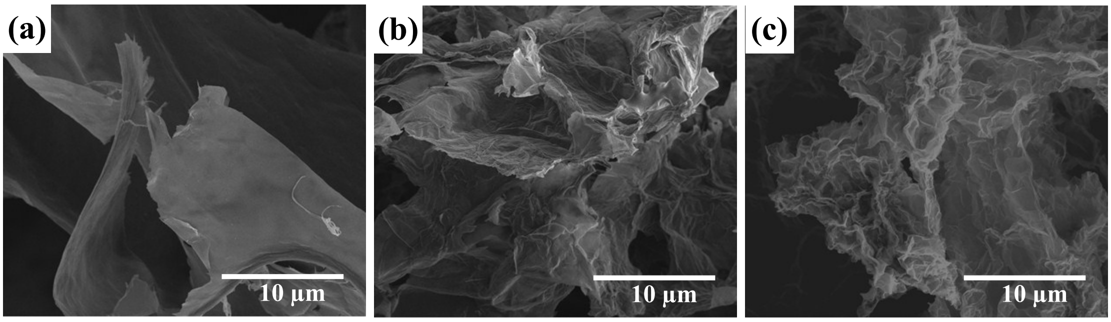

Figure S3. High-resolution SEM images of PGCSs with PEDOT:PSS to GO weight ratios of (a) 6:0, (b) 3:3 and (c) 0:6, corresponding to PS, PGCS-2 and GS, respectively.

Table S1. Comparison of surface area, pores volume and pore width.

Sample	Initial PEDOT:PSS to GO ratio	BET surface area ($m^2\ g^{-1}$)	BJH pores volume ($cm^3\ g^{-1}$)	BJH pore width (nm)
PS	6:0	2.35	0.0044	39.5
PGCS-1	4:2	4.80	0.0114	7.50
PGCS-2	3:3	11.3	0.019	6.78
PGCS-3	2:4	14.7	0.051	6.09
GS	0:6	57.6	0.103	4.71

As evident from Table S1, with an increase in GO content, the resultant composites exhibit a larger surface area, higher pores volume, and smaller pore width, which further verified the tunable porous structure with different PEDOT:PSS to GO ratio.

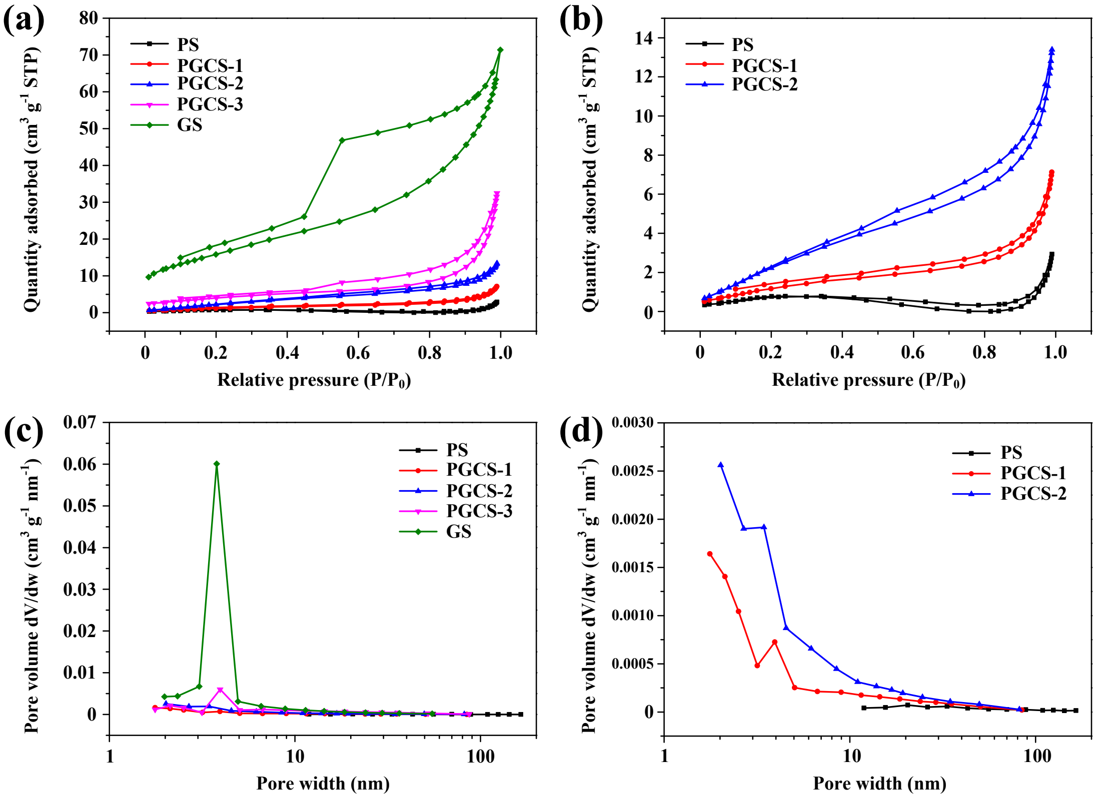

Figure S4. Nitrogen adsorption–desorption isotherms at standard temperature and pressure (STP): (a) comparison among PS, PGCS-1, PGCS-2, PGCS-3, and GS, (b) detailed view of PS, PGCS-1 and PGCS-2. The corresponding Barrett-Joyner-Halenda (BJH) model pore size distribution curves, where dV/dw refers to the rate of change of pore volume with respect to pore size, (c) comparison among PS, PGCS-1, PGCS-2, PGCS-3 and GS, and (d) detailed view of PS, PGCS-1 and PGCS-2.

As shown in Figure S4a, GS shows a much higher gas adsorption than other samples, whereas the PS exhibits the lowest adsorption. The adsorption decreases with the increasing of PEDOT:PSS content, indicating an increase of the surface area with the addition of GO content. GS and PGCS-3 feature typical type IV isotherm according to the classification by the International Union of Pure and Applied Chemistry (IUPAC). The distinct hysteresis loop at the relative pressure ratio P/P$_0$ value from 0.45 to 1.0 indicates the existence of an abundant of mesopores.[1,2] PGCS-1 and PGCS-2 exhibit type IV isotherm with a hysteresis loop at a high relative pressure between 0.55 and 1.0, suggesting the presence of both mesopores and macropores. As shown in Figure S4b, the shape of the hysteresis loop of PGCS-1 and PGCS-2 is of type H3, indicating the existence of slit-shaped pores, which may be caused by large and flat sheets formed by PEDOT chains.[3,4] The isotherm of the PS shows a decrease at the P/P$_0$ value from 0.3 to 0.8 and overall poor nitrogen adsorption, indicating the lack of mesopores. Furthermore, as shown in the Figure S4c and d, the main pore size distributions obtained from the Barrett-Joyner-Halenda (BJH) method of GS and PGCS-3 have significant peaks at 3.79 and 3.95 nm respectively showing much higher pore volume than other samples. Different from GS and PGCS-3, PGCS-1 and

PGCS-2 exhibits a broader peak range from 1.76 to approximately 6 nm with pore width ranging from 1.76 to 84.5 nm, whereas PS shows even broader pore size distribution ranging from 12 to 165 nm. This indicates that, with increasing GO content, the composite tends to form a uniform microstructure with small pore size.

Figure S5. Effect of the PEDOT:PSS to GO weight ratio on the size of the resultant low-profile sponges. From left to right: blank glass mold, PS, PGCS-1, PGCS-2, PGCS-3 and GS.

As evident in the Figure S5, with the decrease of PEDOT:PSS, the resultant sponge become larger. This is because HI can only partly remove the hydrophilic PSS from PEDOT:PSS, which may hinder the process of self-assembly. The remaining hydrophilic PSS in the composite further causes additional expansion during DI water washing and ammonia treatment.

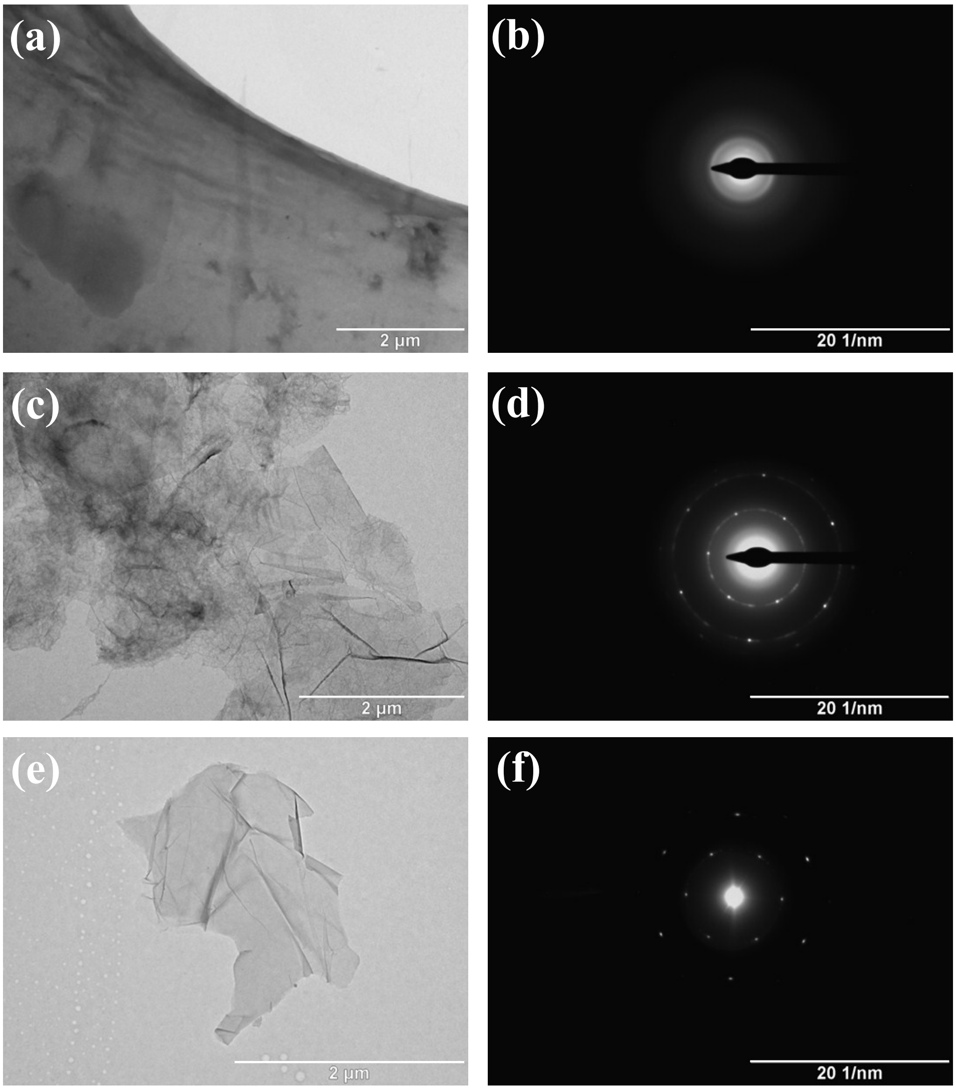

Figure S6. TEM images and the corresponding selected area electron diffraction (SAED) of (a-b) PS, (c-d) PGCS-2, and (e-f) GS.

As can be seen in Figures S6a and b, PS contains a large and flat sheet. The SAED shows a broad diffused spot, exhibiting the typical amorphous, polymeric structure of PEDOT:PSS. Figure S6e shows a typical wrinkled graphene sheet of GS. Figure S6f shows the typical SAED image of graphene with sharp and hexagonal patterns. As shown in Figure S6c, PGCS-2, being a composite of PEDOT:PSS and rGO, exhibits wrinkles similar to GS, but with a much smaller sheet size than PS. The SAED of PGCS-2 (Figure S6d) features both a central diffused spot and a hexagonal pattern, expectedly suggesting the combination of PEDOT:PSS and rGO.

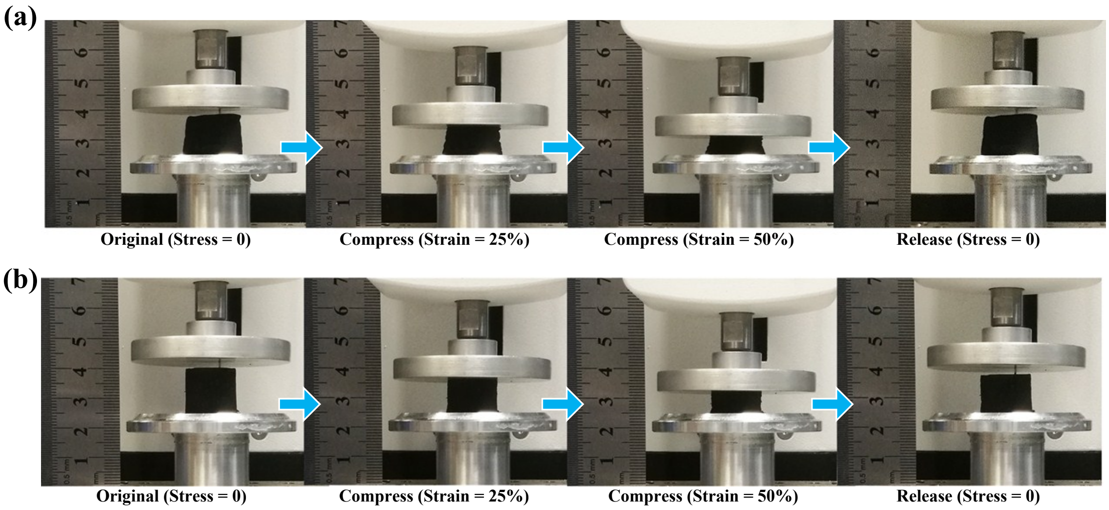

Figure S7. A set of real-time images of PS (a) and GS (b) during the original, compressed (under strain of 25% and 50%) and released states.

As shown in Figure S7, PS can almost fully recover from the compression (Figure S7a) showing a good compressibility due to the 3D porous structure and robust interconnection of the elongated and crystallized PEDOT:PSS chains. Moreover, as can be seen in Figure S7 and Fig. 3c, different from GS, both PS and PGCS-2 exhibit greater buckling during compression. This is due to the long chain structure and specific orientation of crystallized PEDOT:PSS chains which can effectively avoid the collapse of pore walls and further structural damage. As shown in Figure S7b, after removing the force, GS still has 15.8% of residual strain in height. This may be due to its randomly oriented porous structure that is susceptible to the increased of internal friction and adhesion among the internal micropores, thus generating microcracks.[5,6]

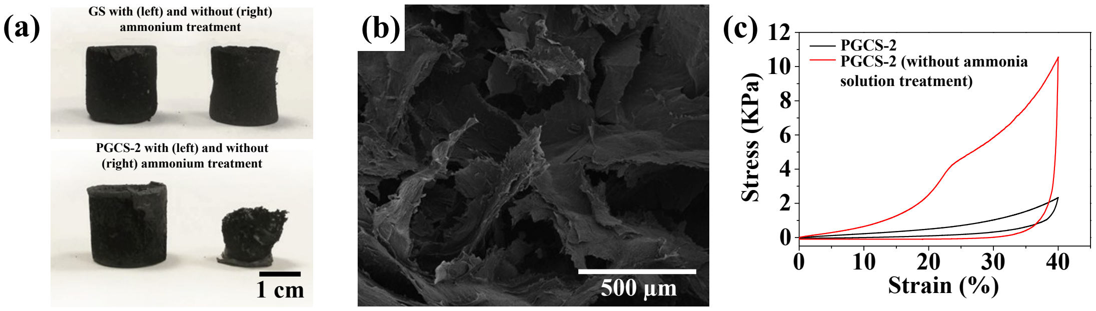

Figure S8. Effect of ammonium treatment on GS and PGCS-2. (a) Photographs illustrations of GS and PGCS-2 with and without ammonium treatment synthesized from conventional glass bottles. (b) SEM image of PGCS-2 without ammonium treatment. (c) Compressive strain-stress curve of PGCS-2 with and without ammonium treatment.

As shown in Figure S8a, for GS and PGCS-2, ammonium treatment enhances the symmetry and uniformity of the overall structure. PGCS-2 without ammonium treatment shows significant distortion. This may be because, compared to GS, PGCS-2 with residual hydrophilic PSS chains has a stronger combination with water, causing its microstructure to be more readily destroyed by the expansion of ice during freeze drying without ammonium treatment. The SEM image of PGCS-2 without ammonium treatment (Figure S8b) further shows poor and irregular microstructures caused by unrestricted ice expansion. Figure S8c shows the compressive strain-stress performances of PGCS-2 with and without ammonium treatment. It is evident that PGCS-2 without ammonium treatment occupies a much larger strain-stress curve area and a higher stress, indicating a poor resilience and uniformity.

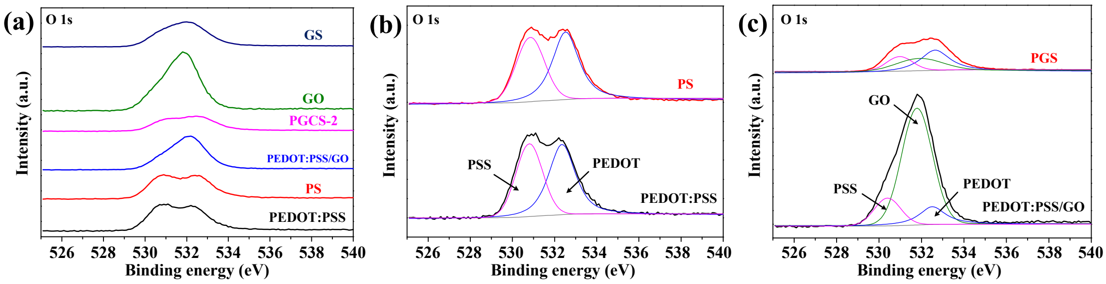

Figure S9. XPS spectra of O 1s in 3D PGCS.

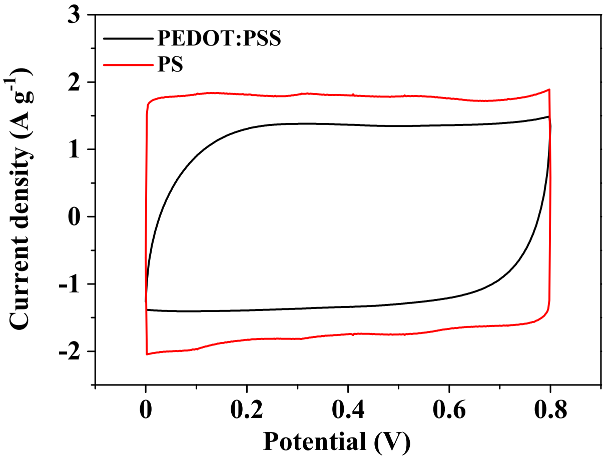

Figure S10. Comparison of CV curves between the pristine PEDOT:PSS and the PS electrodes obtained at the scan rate of 50 mV s^{-1}.

As can be seen in Figure S10, the CV curve of PS electrode is much more rectangular and larger than that of the pristine PEDOT:PSS electrode, due to the removing of PSS chains and the elongation of coiled PEDOT chains under HI treatment.

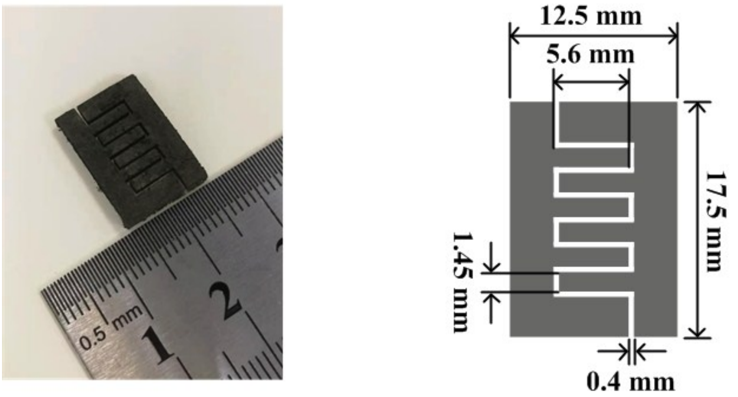

Figure S11. The photograph of the laser patterned PGCS interdigitated electrode (left) for MSC device and the corresponding schematics (right).

Details of the laser patterned interdigitated electrodes are shown in Figure S11. The width and gap of the electrodes are 1.45 mm and 0.4 mm, respectively. The effective thickness of the electrode above silicone rubber is about 0.66 mm.

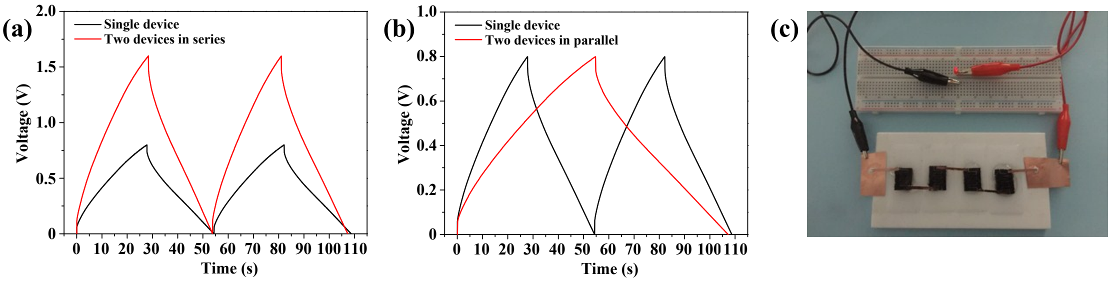

Figure S12. GCD curves of two (a) series and (b) parallel devices at the current density of 500 μA cm^{-2}. (c) Optical image of a red LED powered by four charged MSCs connected in series.

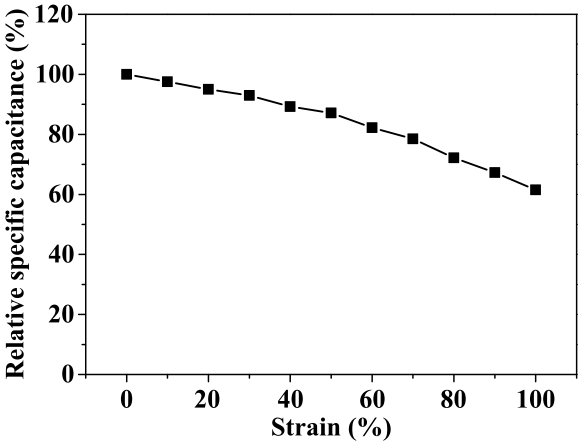

Figure S13. MSC capacitance across strain levels.

Table S2. Comparison of stretchable supercapacitors.

Active material	**Substrate**	**Electrolyte**	**Areal specific capacitances (mF cm^{-2})**	**Maximum stretchability**	**Cycling stability**	**Capacitances retention under stretching**	**Ref.**
3D PGCS	Silicone rubber	PVA/H_2SO_4	11.18 under scan rate of 50 mV s^{-1}	100%	5 000 cycles (88.6% retention)	87.1% under 50% strain	This work
LIG	PDMS	PVP/NaCl	0.65 under scan rate of 50 mV s^{-1}	50%	5 000 cycles (92% retention)	84% under 50% strain	7
Layered graphene	PDMS	PVA/H_3PO_4	0.54 under scan rate of 500 mV s^{-1}	100%	10 000 cycles (96% retention)	92% under 50% strain	8
LIG/PEDOT:PSS	Silicone rubber	PVA/H_3PO_4	0.79 under discharge current of 50 µA cm^{-2}	400%	10 000 cycles (96% retention)	63.9% under 100% strain	9

References

1. J. Ji, Y. Li, W. Fu, Z. Cui, J. Shen and M. Ye, *Journal of Colloid and Interface Science*, 2017, **505**, 983–994.
2. J. Lykiema, K. S. W. Sing, J. Haber, M. Kerker, E. Wolfram, J. H. Block, N. V. Churaev, D. H. Everett, R. S. Hansen, R. A. W. Haul, J. W. Hightower and R. J. Hunter, 1984, 17.
3. Y. Li, W. Ho, K. Lv, B. Zhu and S. C. Lee, *Applied Surface Science*, 2018, **430**, 380–389.
4. Z. Zhang, Y. Zhang, L. Lu, Y. Si, S. Zhang, Y. Chen, K. Dai, P. Duan, L. Duan and J. Liu, *Applied Surface Science*, 2017, **391**, 369–375.
5. C. Wang, X. Chen, B. Wang, M. Huang, B. Wang, Y. Jiang and R. S. Ruoff, *ACS Nano*, 2018, **12**, 5816–5825.
6. C. Zhu, T. Y.-J. Han, E. B. Duoss, A. M. Golobic, J. D. Kuntz, C. M. Spadaccini and M. A. Worsley, *Nat Commun*, 2015, **6**, 6962.
7. A. Lamberti, F. Clerici, M. Fontana and L. Scaltrito, *Advanced Energy Materials*, 2016, **6**, 1600050.
8. D. Qi, Z. Liu, Y. Liu, W. R. Leow, B. Zhu, H. Yang, J. Yu, W. Wang, H. Wang, S. Yin and X. Chen, *Advanced Materials*, 2015, **27**, 5559–5566.
9. W. Song, J. Zhu, B. Gan, S. Zhao, H. Wang, C. Li and J. Wang, *Small*, 2018, **14**, 1702249.